1988A&A...205...29B

Astron. Astrophys. 205, 29–40 (1988)

ASTRONOMY
AND
ASTROPHYSICS

A multifrequency radio continuum survey of M 33

II. Thermal and non-thermal emission

U. R. Buczilowski

Max-Planck-Institut für Radioastronomie, Auf dem Hügel 69, D-5300 Bonn 1, Federal Republic of Germany

Received February 1, accepted April 2, 1988

Summary. The galactic radio continuum emission of M 33 at 17.4 cm, 11.1 cm, 6.3 cm, and 2.8 cm wavelength is investigated after subtraction of background sources. The integrated spectrum of the Effelsberg measurements between 35.6 cm and 6.3 cm is steeper ($\alpha = 0.91 \pm 0.13$, $S \propto \nu^{-\alpha}$) than for most other spiral galaxies. The radio emission is separated into non-thermal and thermal components. The latter contributes $29 \pm 16\%$ and $48 \pm 29\%$ to the total intensity at 6.3 cm and 2.8 cm respectively. The synchrotron emission appears to be more smoothly distributed than the thermal emission and reveals global similarities with the distribution of the known supernova remnant (SNR) candidates.

The radial profiles of the thermal radio emission and SNR candidates are much steeper than those of the non-thermal emission and its linearly polarized fraction. If the relativistic electrons originate in SNRs, they must propagate radially over a distance of ≈ 6 kpc. At the assumed corotation radius of $r = 13'$ several radial profiles show discontinuities.

Various constituents of M 33 are distributed asymmetrically with respect to the minor axis. The northern part has a distinctly higher polarized fraction and slightly more thermal emission than the southern part; however, the latter has more non-thermal emission and a somewhat steeper spectrum.

Previous investigations have shown the existence of a shock front, HI and dust associated with the main southern spiral arm (IS). Similar conditions appear to exist in arm IVS. In both cases radio continuum emission peaks, displaced by ≈ 200 pc towards the inner edges, are evident.

Key words: spiral galaxies – M 33 – radio continuum – free-free emission – synchrotron radiation – cosmic rays – density waves

1. Introduction

The nearby spiral M 33 (NGC 598) is a remarkable galaxy in several respects; it has a large number of SNR candidates, a rather low optical luminosity and a patchy spiral structure with indications of both density waves and stochastic self-propagating star formation.

This is the second in a series of papers dealing with radio continuum measurements of M 33 at 21.1 cm, 17.4 cm, 11.1 cm, 6.3 cm, and 2.8 cm carried out with the Effelsberg 100-m telescope. In Paper I (Buczilowski and Beck, 1987) the telescope, receiver and measurement parameters were given, as well as the basic distributions of total and linearly polarized intensity. In a 2° × 2° field 8 point sources were classified as part of M 33 and 30 as belonging to the background. For most of these 38 objects radio spectra are known.

In Sect. 2 of this paper the total radio emission is studied, for which purpose the background sources are separated from the galactic emission. The integrated spectrum between 35.6 cm and 2.8 cm, using existing low frequency Effelsberg measurements (Beck, 1979), is presented in Sect. 3. The next sections of the paper focus on various constituents and properties of the galaxy. The integrated spectrum and the spectral index distribution between 17.4 cm and 6.3 cm (Sect. 4) are used to separate the total radio emission into thermal and non-thermal components. The thermal content of spiral galaxies at cm wavelengths is still under debate (Gioia et al., 1982; Israel and van der Hulst, 1983) and is derived for M 33 in Sect. 5. The radial profiles of the total, thermal, non-thermal and polarized emission, and of the number surface density of SNR candidates are discussed in Sect. 7. In Sect. 8 global asymmetries in the distributions of thermal, non-thermal and polarized emission, SNR candidates and spectral index are analysed. In Sect. 9 the results for M 33 are discussed with respect to the thermal fraction, origin of cosmic ray electrons and star formation.

2. Radio continuum emission from M 33

Because of its large angular extent, the emission of M 33 is contaminated by a number of background sources. Using the spectral indices and the catalogue of H II regions (Boulesteix et al., 1974) we can reliably classify the emission from unresolved sources in the field (see Paper I, Table IV). To compare the integrated total flux densities of M 33 at various wavelengths the same background sources had to be subtracted from all maps. Point sources with flux densities greater than 0.6% of the expected integrated flux density of M 33 (Beck, 1979) at at least one frequency (i.e. S 1, 3, 4, 7, 9, 11–24, 30, 31, 37, and 38 in the total 2° × 2° field) were subtracted from all fields. Extrapolated flux densities were taken from the source spectra fits given in Paper I. The remaining 7 fainter background sources (S 2, 28, 32–36) were, if visible, subtracted from individual maps to improve the base-level.

The radio emission of M 33 at 17.4 cm thus derived is presented in Fig. 1. For easy comparison of the cleaned total power maps and those in Paper I the same contour intervals were chosen. At a distance of 720 kpc (de Vaucouleurs, 1978) the half-power beam width (HPBW) of 7.′7 at 17.4 cm corresponds to 1.6 kpc along the

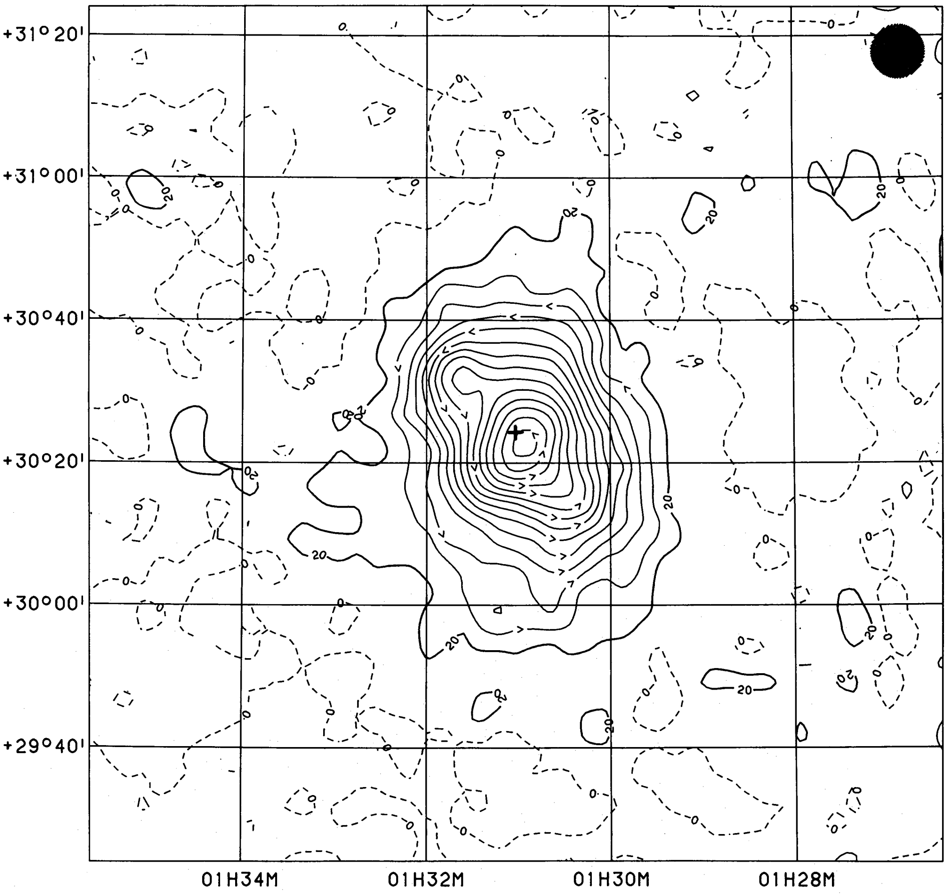

Fig. 1. Distribution of the total intensity of M 33 at 17.4 cm after subtraction of 25 unrelated sources. Contours are shown in equal steps of 20 mJy/b.a. (2.3 δ). The optical centre at $\alpha_{50} = 1^{\rm h}31^{\rm m}01\overset{\rm s}{.}67$ and $\delta_{50} = 30°24'15''$ (de Vaucouleurs and Leach, 1981) is marked by "+" in all figures

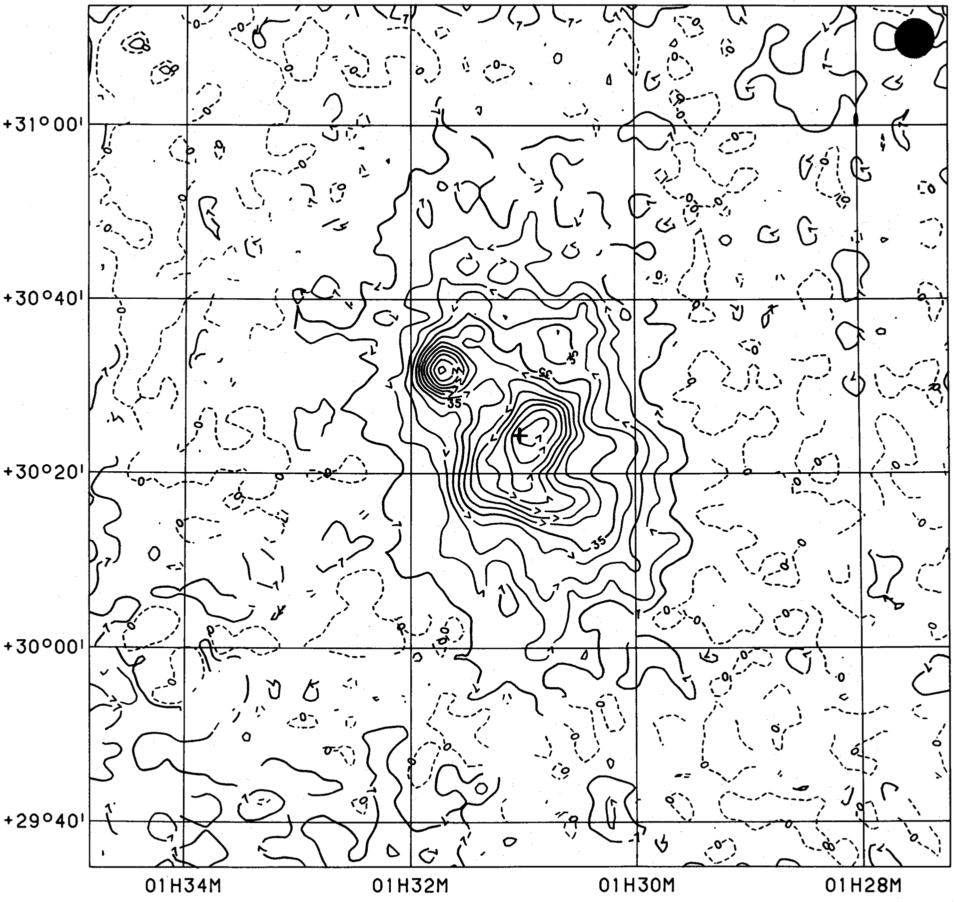

Fig. 2. Distribution of the total intensity of M 33 at 11.1 cm after subtraction of 20 unrelated point sources. Contours are shown in equal steps of 7 mJy/b.a. (2.3σ)

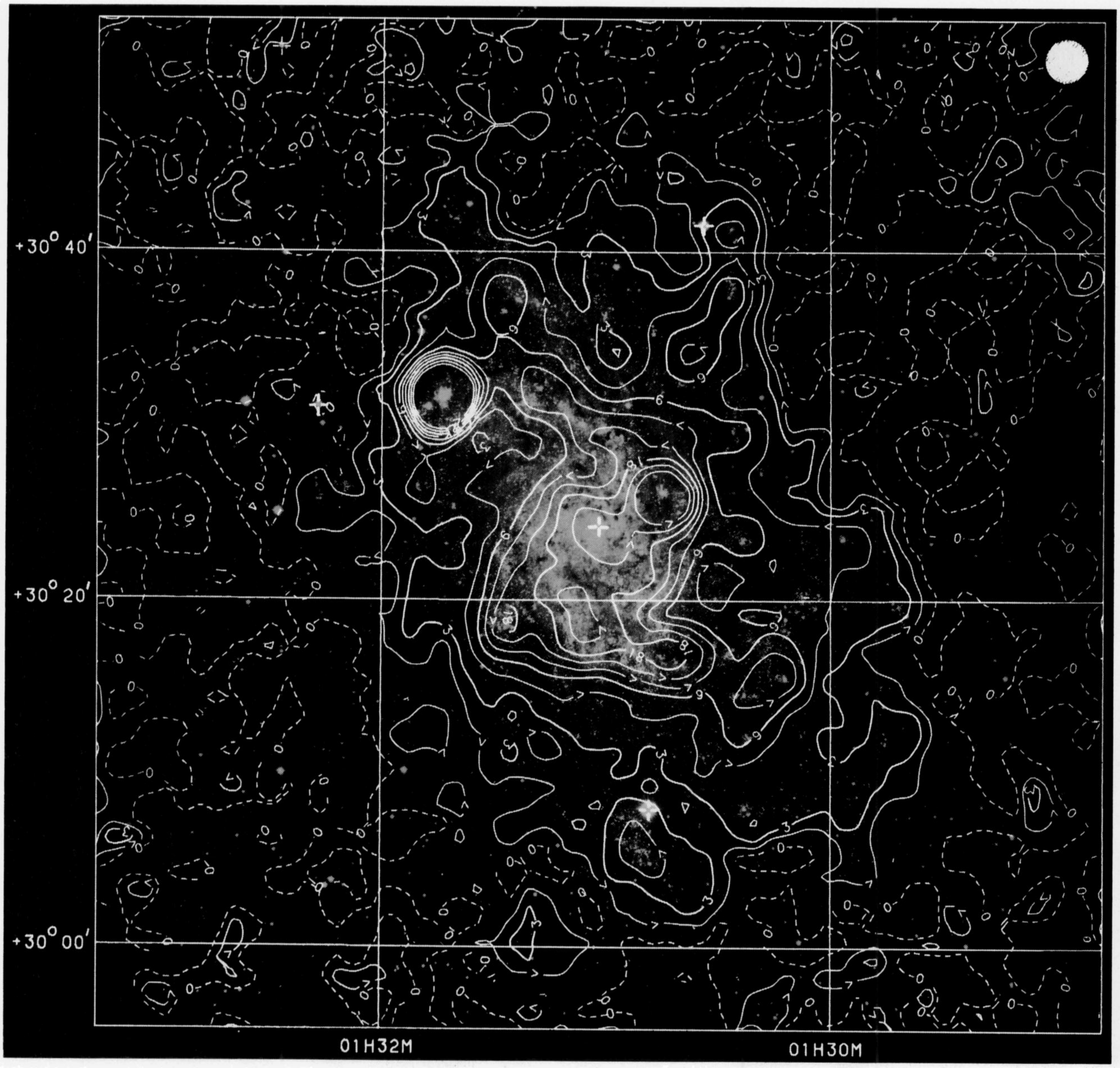

Fig. 3. Distribution of the total intensity of M 33 at 6.3 cm after subtraction of 9 unrelated point sources. Contours start at 1.5 mJy/b. a. (2.2σ) and are overlayed onto an optical picture (Lick Observatories)

major axis and 2.8 kpc along the minor axis, using position angle p.a. = 21° and inclination $i = 55°$. Optically M 33 has 2 dominant inner arms (IN and IS) and 8 weaker outer arms (notations of Humphreys and Sandage, 1980, cf. Fig. 1 in Paper I). At 17.4 cm an extended galactic disk with intensity decreasing radially outwards is evident. The brightest H II region of M 33, NGC 604, is visible to the northeast of the centre and indicates the position of the northern main arm IN.

With a resolution of 4.′4 (920 pc × 1600 pc) at 11.1 cm the 2-arm spiral structure of IN and IS is apparent (Fig. 2). NGC 604 is clearly separated and arms IIIN, IVN, VN, IIIS, IVS and VS are indicated by fragmented emission.

The emission of M 33 at 6.3 cm is shown superimposed onto an optical picture in Fig. 3. The central region, an association of small, luminous H II regions (see Boulesteix et al., 1974; Courtés et al., 1987), is not conspicious. This is in agreement with the finding of Hummel (1981) that in the progression from early to late-type spirals (M 33 is classified Scd) the contribution of the central ≈ 1 kpc to the total radio luminosity appears to decrease.

The radio disk at 6.3 cm extends over 50′ × 30′ (2σ level), thus including the outer regions of the galaxy. With the resolution of 2.′4 (510 pc × 880 pc) most of the disk exhibits spiral structure. Arm IN shows weaker radio emission than its southern counterpart IS. Also the less luminous arms in the north (IIIN, IVN, VN) can clearly be seen. The southern outer arms IIIS–VS appear only as fragmented 6.3 cm emission.

Some common features of the optical and 6.3 cm radio emission are noteworthy. Most obvious is the radio continuum emission from IVS around $\alpha_{50} = 1^{\rm h}30^{\rm m}\!.8$, $\delta_{50} = 30°05'$, which coincides with the OB associations HS 110 andd HS 112 (Humphreys and Sandage, 1980) and the H II regions B 246–B 251, Z 47–Z 49, Z 52, Z 52 A (Courtés et al., 1987). The regions of peak flux

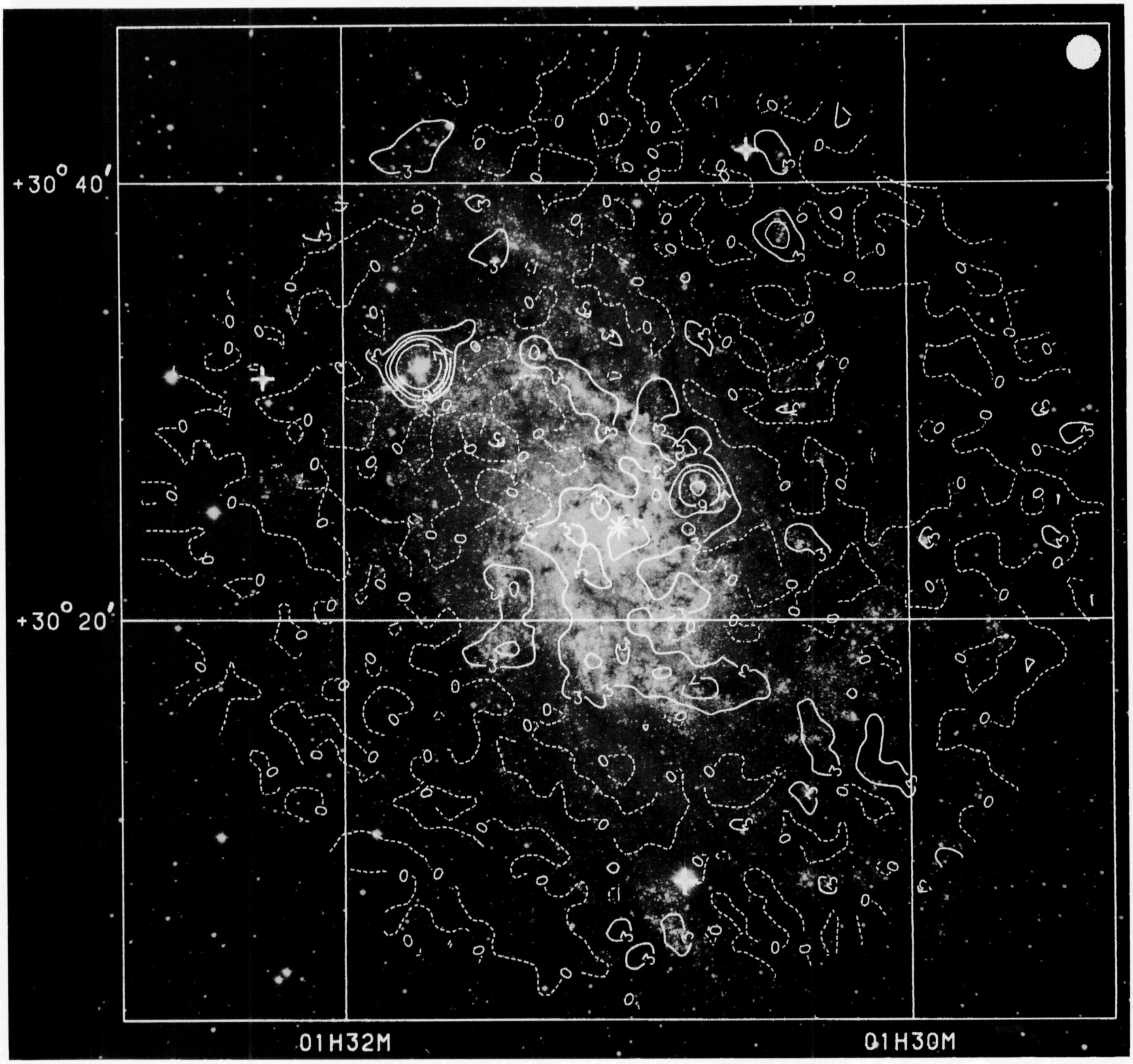

Fig. 4. Distribution of the total intensity of M33 at 2.8 cm smoothed to a 1.′5 beam after subtraction of 2 unrelated point sources. Contours starting at 3 mJy/b.a. (2.5σ) are overlayed onto the optical picture

density in IS are situated along the inner edge of the optical arm as is the local peak at $\alpha_{50} = 1^{\rm h}31^{\rm m}.4$, $\delta_{50} = 30°19'$ compared to its optical counterparts, the luminous H II regions B 710–714 and OB association HS 101. Emission from the brightest H II regions (see Fig. 8 for an identification) NGC 604, NGC 595 and IC 132 is clearly indicated, but that from NGC 588, NGC 592, IC 133, and IK 53 is weak. The radio source associated with NGC 604 is slightly extended in the north-south direction.

The 2.8 cm map is presented in Fig. 4 as an overlay onto the optical plate. With the available sensitivity the disk emission is hardly measurable. However, the arms IS and (fainter) IN are delineated and there is weak emisssion from the central region. Emission from the dominant H II regions NGC 604 and NGC 595 is extended with respect to the 1.′5 beam, that from NGC 604 again in north-south direction. The sources IC 132, IC 133, and IK 53 are clearly visible. Some optically bright regions correspond to enhancements in radio emission, e.g. the termination of arms IVS and IIIN. Remarkable in the southern section is the alignment of 4 of the 5 radio continuum peaks along the inside edges of the nearest optically bright regions, confirming the indications at 6.3 cm. In contrast, the radio emission from the main northern arm appears to originate along its outer edge.

3. Integrated flux densities and spectrum

Fifteen values of the integrated radio flux density of M 33 between 94.3 cm (318 MHz) and 6.2 cm (4850 MHz) have already been

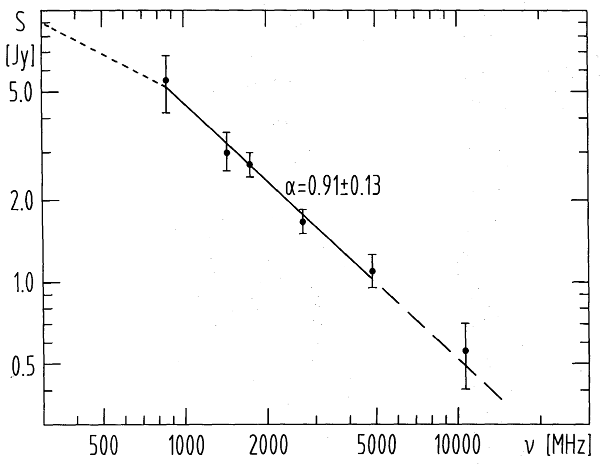

Fig. 5. Radio spectrum of the integrated emission from M 33. The spectral index was computed for the range 842 MHz to 4750 MHz (35.6 cm to 6.3 cm). The dashed line is an extrapolation. The shorter dashes indicate the expected flatter spectrum for the low frequency part (318 MHz–842 MHz) using two further values (Beck, 1979)

published (see tables in von Kap-herr et al., 1978; Beck, 1979). However, differences between telescopes, angular resolutions, calibration scales and areas integrated have so far prevented the construction of a reliable spectrum of integrated emission. Von Kap-herr et al. (1978) subtracted the two main background sources (S 3, 9) and found a spectral index $\alpha = 0.52 \pm 0.08$ for the 94.3 cm to 6.2 cm range. Next, Beck (1979) removed all visible background sources and adjusted the calibration scales but unfortunately also had to use different integration areas. For the same frequency range he obtained $\alpha = 0.66 \pm 0.06$.

However, the data are also consistent with a relatively flat spectrum between 94.3 cm and 35.6 cm ($\alpha = 0.2 \pm 0.2$) and a steeper section between 21.1 cm and 6.2 cm ($\alpha = 0.8 \pm 0.2$). The spectrum beyond 30 cm (1 GHz) may be related to a break in the cosmic ray electron spectrum between 3 GeV and 6 GeV assuming a magnetic field strength of $4 \pm 2\,\mu$G (Buczilowski, 1985) in the formula of Webber et al. (1980). Spectral breaks beyond 30 cm have also been confirmed for NGC 253 (Reynolds and Harnett, 1983, and Fig. 4 in Klein et al., 1983), M 51 (Klein et al., 1984), M 101 and possibly IC 342 (Gräve, 1984).

With respect to calibration, integrated area and subtracted background (Sect. 2) all Effelsberg maps of M 33 were treated in the same way. The total flux density was integrated in ellipses around the optical centre out to $r_{\max} = 50'$ on the major axis (10.5 kpc), thus exceeding the Holmberg radius of $r = 8.7$ kpc. Baselevels were obtained between $r = 60'$ and $r = 70'$. However, the 2.8 cm map could be integrated only to $r_{\max} = 22\rlap{.}'5$ (thus providing a lower limit to the total flux density). So the comparable value for $r_{\max} = 50'$ was extrapolated using the radial profile at 6.3 cm and the spectral index. Errors in flux densities were calculated following the formula given by Klein and Emerson (1981). In addition, the calibration error at 35.6 cm (taking into account Bystedt et al., 1984) was increased to 15%, the systematic error for the H I-corrected 21.1 cm map and the baselevel error at 2.8 cm were doubled. Table 1 lists the resultant 6 flux densities.

The integrated spectrum is displayed in Fig. 5. A linear fit over the 35.6 cm to 6.3 cm range gives a spectral index of $\alpha = 0.91 \pm 0.13$. The dispersion of the flux densities around the fitted line is low, with the 6.3 cm and 2.8 cm values slightly above the straight line, indicating a flattening of the spectrum. Compared to those of many other spiral galaxies, the spectrum of M 33 in the investigated range is rather steep. Gioia et al. (1982) found $\alpha = 0.74 \pm 0.12$ for 56 bright spirals, however, between 73.5 cm and 2.8 cm.

4. Spectral index distribution

To determine the spectral index distribution in M 33, the cleaned radio continuum maps at 17.4 cm, 11.1 cm, and 6.3 cm were smoothed to the common beam width of $7\rlap{.}'7$, restricted to a common size and interpolated onto the same grid. Baselevels of the three maps were matched using doubly logarithmic I_1–I_2 diagrams. For each point in the map a straight line was fitted to the three intensities. Spectral indices were computed only at those positions, for which the flux density was at least twice the rms noise σ at each frequency. The resultant spectral index distribution is shown in Fig. 6. Typical errors increase from ± 0.08 near the centre to ± 0.22 in the outer regions of the galaxy.

The spectral index is relatively low in the nuclear region and at the positions of the H II regions NGC 604, NGC 595, NGC 588 and IC 133. The mean spectral index is lower in the northern half than the southern one. The derivation of the spectral index distribution between 6.3 cm and 11.1 cm would allow a resolution of $4\rlap{.}'4$, but is too unreliable due to the small range in wavelength. A substantial improvement in the spectral index study of M 33 would be possible by comparison of a more sensitive and larger 2.8 cm Effelsberg map with one at 49.2 cm or 91.7 cm from the Westerbork interferometer.

Table 1. Integrated total flux densities of M 33. The thermal fractions are given for a non-thermal spectral index of $\alpha_{\rm nth} = 1.1$ (Sect. 5)

λ/cm	ν/MHz	map size/'	$r_{\max}$/'	base/'	S_{M33}/mJy	f_{th}/%
35.6	842	120x120	50	60-70	5377±1217	7± 3
21.1	1420	120x120	50	60-70	2990± 440	11± 5
17.4	1720	120x120	50	60-70	2714± 254	12± 6
11.1	2702	99x 99	50	60-70	1683± 168	19±10
6.3	4750	100x 70	50	60-65	1100± 167	29±16
2.8	10700	45x 45	22.5	30-35	482± 130	
			50	60-65	550± 150	48±29

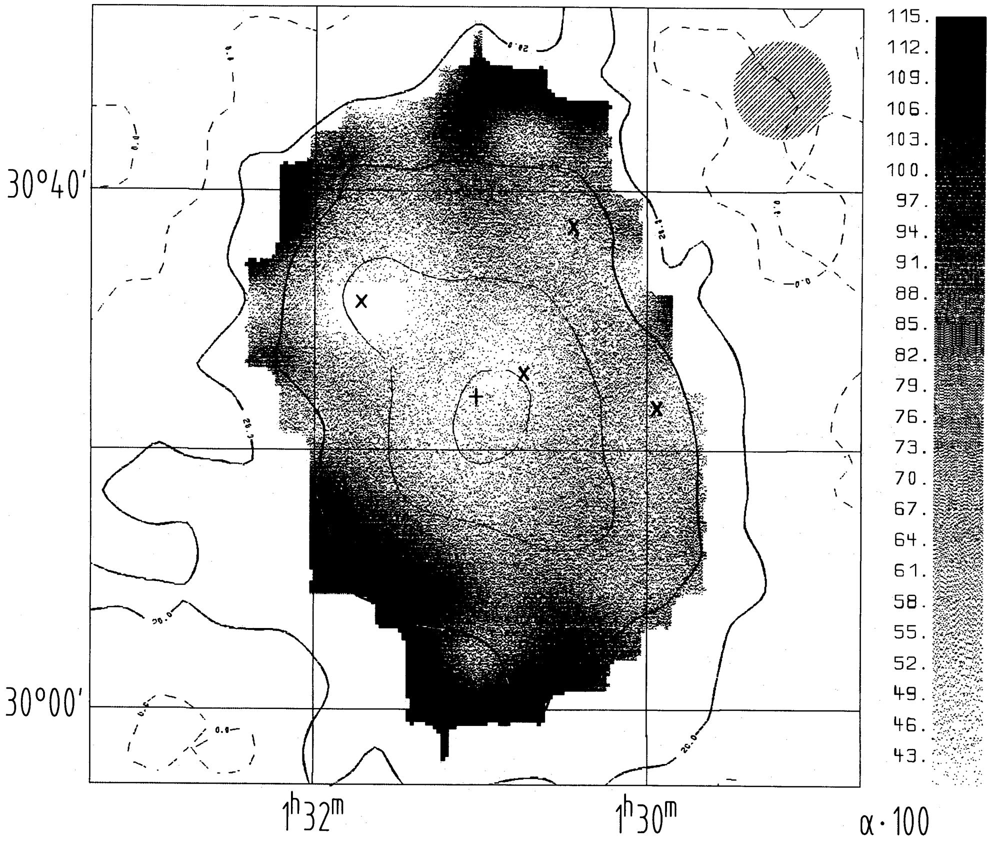

Fig. 6. Grey scale representation of the spectral index distribution with 7.′7 resolution derived by straight line fits to the 17.4 cm, 11.1 cm and 6.3 cm data points. Also shown are some contours of the 17.4 cm emission (comparable with Fig. 1). Crosses ("X") mark the H II regions NGC 604, NGC 595, IC 133 and NGC 588, starting at the left-hand side

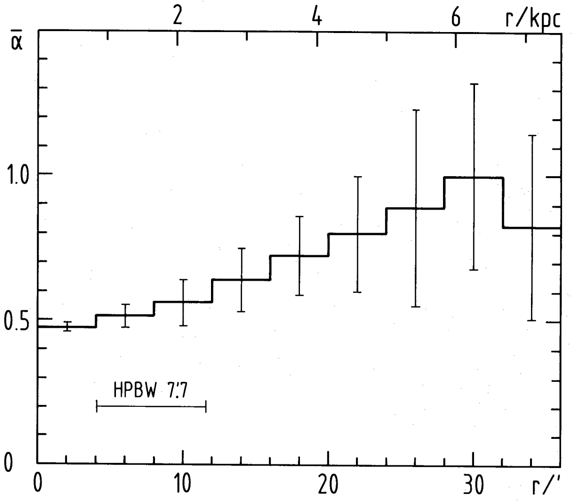

Fig. 7. Radial distribution of the spectral index between 6.3 cm and 17.4 cm in ellipses of 4′ width on the major axis. Error bars correspond to one standard deviation

To obtain the radial distribution of the spectral index the three input maps were integrated in ellipses. The three data sets ($\log \bar{I}, \log \nu$) were fitted with weights according to the square of the mean signal-to-noise ratio. The radial profile is presented in Fig. 7. The spectral index rises monotonically from the centre to a radius $r = 30'$.

Within the 35′ radius, where H II regions have been detected (Boulesteix et al., 1974), the spectral index is the result of a combination of thermal and non-thermal emission. Thus, assuming a constant non-thermal spectral index, variations in Fig. 6 are explained solely by those of the thermal fractions and the increasing value in Fig. 7 can be interpreted as a general decrease of the thermal fraction with radius.

5. Thermal emission

If the integrated spectrum is produced by the combination of a thermal component with spectral index $\alpha_{\rm th} = 0.1$ and a non-thermal component with $\alpha_{\rm nth}$, which is constant across the frequency range investigated, analysis of the assumed spectral curvature yields an estimate of $\alpha_{\rm nth}$ and the corresponding thermal fractions $f_{\rm th}$ of the emission (Klein et al., 1984). For the spectrum in Fig. 5 a value of $\alpha_{\rm nth} = 1.10 \pm 0.14$ was found. The uncertainties arise largely from the possible errors in the 2.8 cm flux density. Stated thermal fractions depend severely on the assumed non-thermal spectral index. Hence, the steep synchrotron spectrum derived here implies a thermal fraction $f_{\rm th} \approx 30\%$ at 6.3 cm and $f_{\rm th} \approx 50\%$ at 2.8 cm (Table 1). The 6.3 cm value is in agreement with the estimate of Berkhuijsen (1983) using Hα data.

The M 33 data also offer the possibility of determining $\alpha_{\rm nth}$ and $f_{\rm th}$ from the distribution of spectral index if we additionally assume $\alpha_{\rm nth}$ to be spatially uniform. Beyond about $r = 35'$ the thermal emission from H II regions is negligible and the spectral index becomes representative of the synchrotron emission spectrum. In Fig. 7 the spectral index is less than $\bar{\alpha} = 1.0$ for $r \lesssim 36'$. In consideration of both values, $\alpha_{\rm nth} = 1.0 \pm 0.1$ is used hereafter.

A separation of thermal and non-thermal components at 6.3 cm with a resolution of 7.′7 was performed using the method described by Klein et al. (1982); the resulting distribution of thermal free-free emisssion is shown in Fig. 8. In spite of the low resolution, the thermal emission shows some structure. Peaks are seen at the centre and the H II region NGC 604. The arms IIIN and VN (delineated by IC 133 and IC 132) are more clearly seen in Fig. 8 than in the corresponding total power map. Separate integration of the thermal and non-thermal distributions (Figs. 8 and 9) yields a thermal fraction of nearly 50% at 6.3 cm, more than was derived from the integrated spectrum. The main explanation is that this separation used data from 17.4 cm to 6.3 cm with a mean spectral index of $\bar{\alpha} = 0.65$ within $r \cong 28'$, whereas the analysis of the total spectrum covered the whole range between 35.6 cm and 2.8 cm with $r_{\max} = 50'$ and $\bar{\alpha} = 0.91$, which is a more reliable method. In addition, the separation was only performed for data points with known spectral index, neglecting the prevailing non-thermal emission in the outer regions.

6. Non-thermal emission and supernova remnants

To understand the origin and behaviour of cosmic ray electrons

i) the SNR distribution indicating star formation rate and the distribution of the young population as CR source candidates and

ii) the non-thermal emission as an CR effect

can be investigated.

The distribution in M 33 of the non-thermal emission at 6.3 cm (Fig. 9) was obtained by subtracting the map of thermal emission (Fig. 8) from that of the total emission at 7.'7 resolution. Results for thirty-five optically detected SNR candidates were published by D'Odorico et al. (1980, 1982). Selection effects exist, because not every survey has covered the whole extent of the galaxy. Furthermore, only 13 objects have been confirmed spectroscopically so far (Dopita et al., 1980; Blair and Kirshner, 1985), at least 5 of them also in the radio continuum (D'Odorico et al., 1982), one of them additionally in the X-ray range (Markert and Rallis, 1983).

7. Radial profiles

Comparison of various radial profiles at the same resolution may reveal relationships between galaxy constituents. Therefore, the distributions were smoothed to resolutions of 7.'7 or 2.'4 HPBW and integrated in ellipses (Figs. 10 and 11). Five profiles show a relatively high value when $r = 13'$ compared to their otherwise steady decrease. For the total intensities at 6.3 cm and 2.8 cm this is caused by the large contribution of NGC 604 to the integrated flux densities in the corresponding rings. However, also the distribution of the SNR candidates and that of the polarized intensities at 6.3 cm and 17.4 cm are enhanced near $r = 13'$.

Using $I \propto \exp(-r/l)$ for intensity, the radial scale lengths l, listed in Table 2, were calculated. The influence of resolution on this determination is negligible if the HPBW is smaller than the true scale length (Klein et al., 1982). The mean scale length of the three total intensities is $l = 2.1 \pm 0.3$ kpc. The thermal emission ($l = 1.5 \pm 0.2$ kpc) is more concentrated to the centre than the total emission especially compared with the 17.4 cm map, in which the thermal fraction is small. Berkhuijsen (1983) determined the distribution of the thermal component of M 33 at 6.2 cm from the catalogue of detected H II regions in Hα (Boulesteix et al., 1974), where diffuse emission in between individual sources is not included. Then Berkhuijsen and Klein (1985) derived a thermal scale length $l = 1.2 \pm 0.1$ kpc, smaller than their non-thermal length and even slightly smaller than the thermal length stated here. The latter difference can be explained by (i) the higher resolution (2.'6) of their thermal distribution and (ii) their inability to detect all of the diffuse thermal emission.

The number surface distribution of SNR candidates has a scale length $l = 1.4 \pm 0.2$ kpc and resembles the profile of the thermal emission. The distribution of the non-thermal emission is smoother (cf. Figs. 8 and 9) and more extended (Fig. 10) than the two of the young population.

Profiles of the polarized emission were fitted after subtraction of the polarized background sources (see Paper I). Because of the clearly asymmetric distribution of the polarized emission in M 33 and the poor signal-to-noise ratio, the values obtained are of limited use. The profiles of polarized emission at 6.3 cm and 17.4 cm are even broader than those of the non-thermal emission. This is probably due to decreasing Faraday depolarization with increasing distance from the centre as might be expected from the steep profile of the thermal emission.

8. Large-scale asymmetries

The centres of the distribution of H I, H II and O stars are offset from the optical centre of M 33 generally by $\approx 2'$ to the southwest (Colin and Athanassoula, 1981; Berkhuijsen, 1983). Cambridge measurements show only small asymmetries in the neutral hydrogen distribution with the SW region slightly more dominant (Wright et al., 1972; Newton, 1980). However, Westerbork measurements at better resolution and with corrections for missing spacings (Deul and van der Hulst, 1986) revealed that $^2/_3$ of the H I is situated in the southern half. On the other hand, in the outer region ($12' < r < 30'$) H I spiral features are more prominent in the northern half (Newton, 1980, see also Fig. 8 in Deul and van der Hulst, 1987).

In this section, properties of M 33 in the areas north and south of the minor axis (see Fig. 9) will be compared within ellipses of a radius $r_{\max}$ on the major axis. The results are given in Table 3. In the radio continuum the domination of the southern half decreases from 59% at 17.4 cm to 51% at 2.8 cm. This is due to the decreasing fraction of non-thermal emission and to the increasing relative contribution of NGC 604 towards shorter wavelengths.

The spectral index distribution between 17.4 cm and 6.3 cm (Fig. 6) is distinctly steeper in the outer regions, particularly in the southern half. Also the integrated spectrum between 35.6 cm and 6.3 cm within $r_{\max} = 50'$ is slightly steeper in the south than in the north.

The northern half has more thermal but less total radio emission and hence a higher thermal percentage at the wavelengths investigated. A statement on the asymmetry of thermal emission depends on the degree of exclusion of giant H II regions: NGC 604 e.g. contributes ~20% of the thermal emission at 6.3 cm.

If the 35 detected candidates are representative for the true SNR distribution, then SNRs are distributed highly asymmetrically: $^2/_3$ would lie in the southern half. Not unexpectedly, the non-thermal emission is stronger here; indeed the peak intensity lies southwest of the optical nucleus (Fig. 9). The results for thermal and non-thermal emission and for the SNR candidates are in agreement with the asymmetries obtained by Beck (1979) and by Berkhuijsen (1983) for $r_{\max} = 28'$.

The distribution of linearly polarized emission at 21.1 cm, 11.1 cm, and 6.3 cm exhibit a striking north-south asymmetry, whereas no significant difference can be detected at 17.4 cm (Paper I and Table 3). Compared to the southern quadrants, the NW region contains less intense but more highly polarized non-thermal emission (Paper I) and only 10% of the known SNR candidates. These pecularities will be discussed in Paper III.

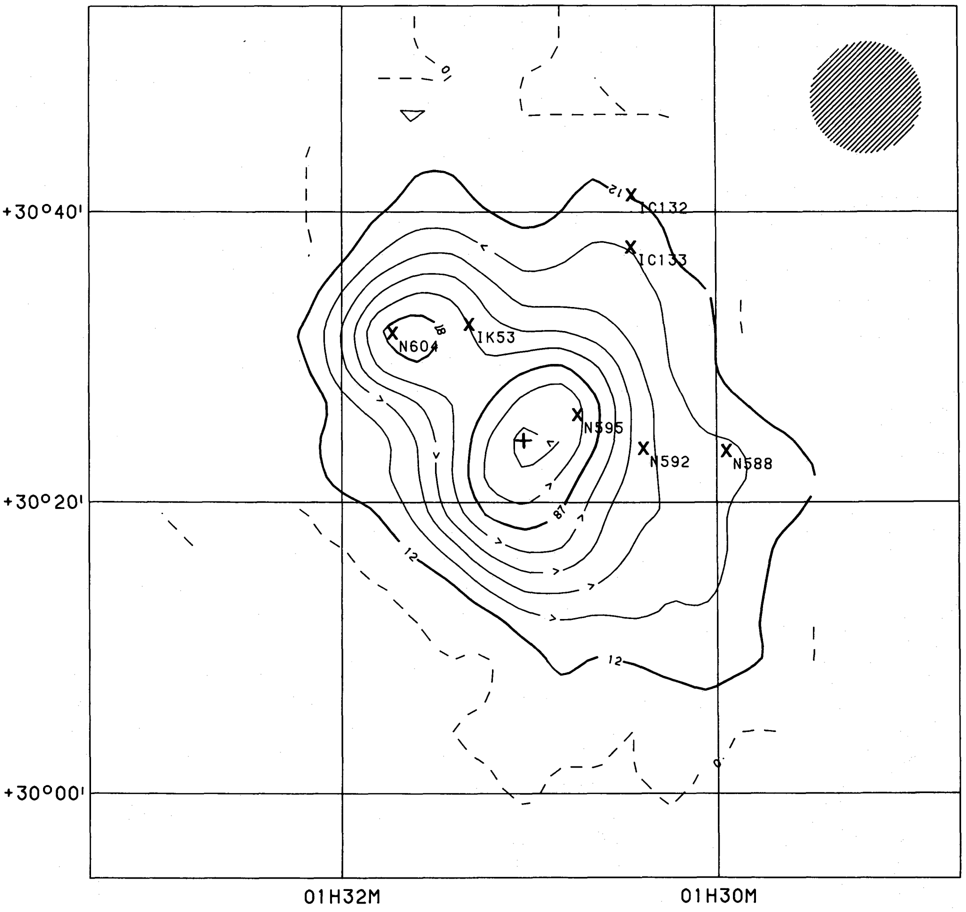

Fig. 8. Thermal emission of M 33 at 6.3 cm with 7.′7 resolution derived from the spectral index distribution. Contours are given in mJy/b.a. The H II regions visible in the fully resolved 6.3 cm map (Fig. 3) are marked

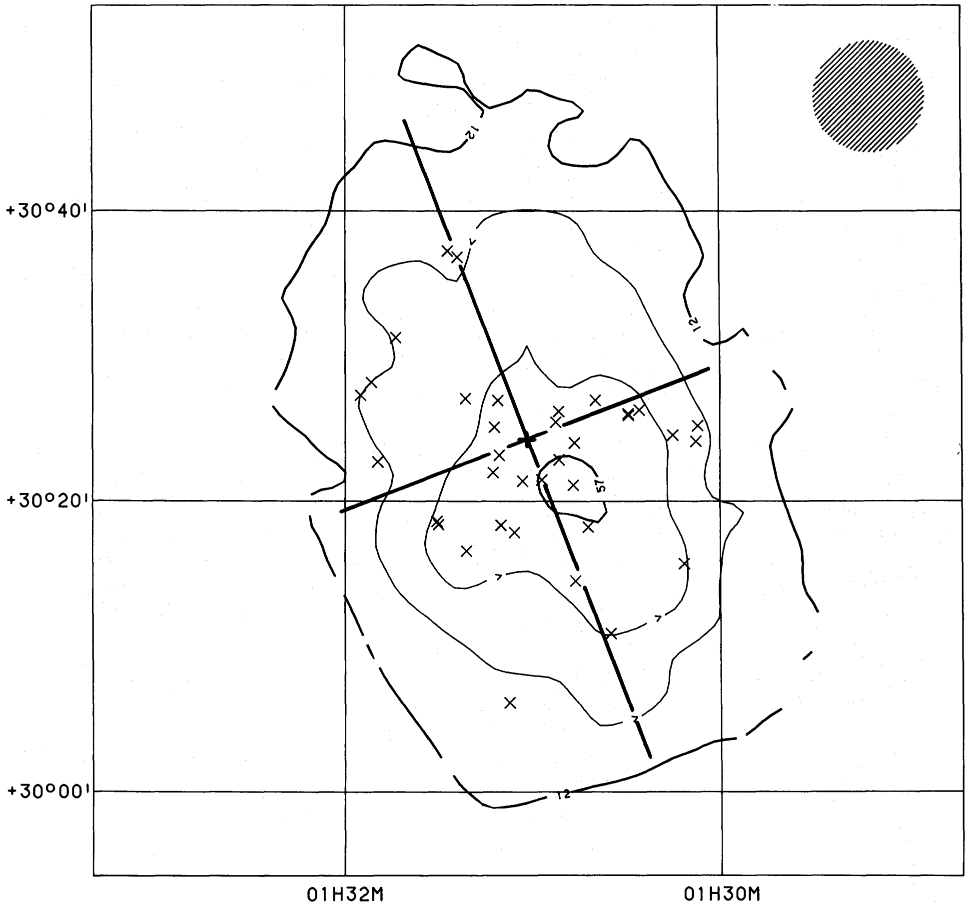

Fig. 9. Synchrotron emission of M 33 at 6.3 cm with 7.′7 resolution derived from the spectral index distribution. Contours are given in mJy/b.a. Optically identified SNR candidates are marked by "×". Major and minor axes are indicated to define halves and quadrants

1988A&A...205...29B

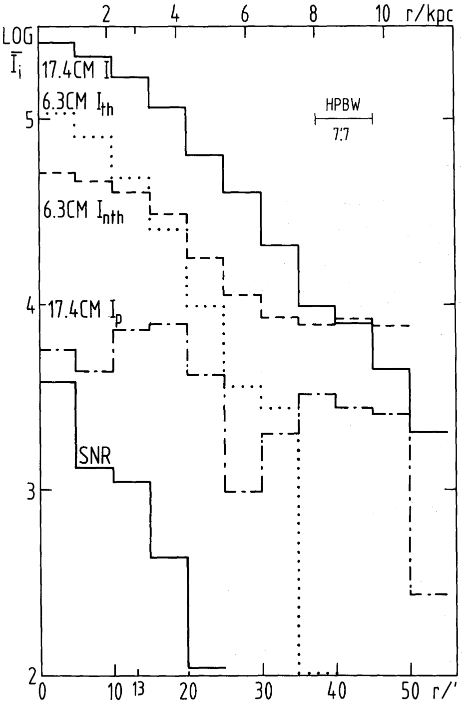

Fig. 10. Radial profiles of total and linearly polarized emission at 17.4 cm and of the thermal and non-thermal component at 6.3 cm. Data at a resolution of 7'.7 were averaged in ellipses of 5' width on the major axis. The number surface density of SNR candidates is given in arbitrary units

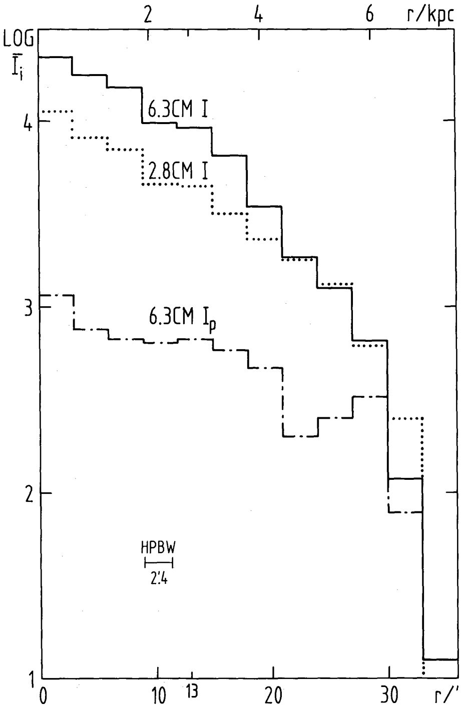

Fig. 11. Radial profiles of total and linearly polarized emission at 6.3 cm and of the total intensity at 2.8 cm at a resolution of 2'.4. The data were averaged in ellipses of 3' width on the major axis

Table 2. Radial scale lengths l in M 33. Conversion to kpc assumes $d = 720$ kpc

Constituent	λ/cm	HPBW/'	r_{max}/'	ℓ/'	ℓ/kpc
SNR candidates			25	6.8± 1.1	1.4±0.2
I	17.4	7.7	55	11.5± 0.8	2.4±0.2
I_p	17.4	7.7	55	38.4±13.8	8.0±2.9
I_{th}	6.3	7.7	40	7.1± 1.0	1.5±0.2
I_{nth}	6.3	7.7	40	17.0± 1.3	3.6±0.3
I	6.3	2.4	36	8.5± 0.7	1.8±0.1
I_p	6.3	2.4	36	18.1± 2.8	3.8±0.6
I	2.8	2.4	36	10.5± 0.6	2.2±0.1

9. Discussion

9.1. *Thermal fraction*

The spectrum of the integrated emission from M 33 between 35.6 cm and 6.3 cm is relatively steep with a spectral index of $\alpha = 0.91 \pm 0.13$. The derived value of the non-thermal spectral index of $\alpha_{nth} = 1.0 \pm 0.1$ coincides with the apparent upper cutoff value for spiral galaxies (Israel and van der Hulst, 1983).

In M 33, thermal emission contributes significantly to the total radio continuum emission: 29 ± 16% at 6.3 cm and 48 ± 29% at 2.8 cm (Table 1). For 56 bright spiral galaxies, predominantly of type Sb and Sc, Gioia et al. (1982) have derived only $f_{th} = 24 \pm 22\%$ at 2.8 cm assuming $\alpha_{nth} = 0.8$. On the other hand, Israel and van der Hulst (1983) detected a distinct flattening in the spectra of 24 spirals at wavelengths less than ≈ 6 cm, especially in the cases of late type spirals. Hence for Sc galaxies they estimated the thermal content at 2.8 cm to be 35 ± 15% ($\alpha_{nth} = 0.75$) or 60 ± 20% ($\alpha_{nth} = 1.0$). As well as M 33, results for two other extensively studied nearby late type spirals (Gräve, 1984) indicate high thermal contents in agreement with the results of Israel and van der Hulst: IC 342 has 23% at 6.3 cm and 40% at 2.8 cm ($\alpha_{nth} = 0.95$); M 101 has 36% at 6.3 cm and 51% at 2.8 cm ($\alpha_{nth} = 0.9$).

In the radio range the thermal emission is independent of the absorption effects that influence the optical emission. Thus a comparison of the calibrated Hα emission with the thermal radio

Table 3. North-South asymmetries in M 33. The percentages are given for the area within ellipses of a radius r_{max} on the major axis

Constituent	r_{max}/′	North/%	South/%
I 17.4 cm	50	41±6	59±6
I 11.1 cm	50	44±5	56±5
I 6.3 cm	50	45±5	55±5
I 2.8 cm	22.5	49±4	51±4
α(6.3 cm–35.6 cm)	50	0.89±0.06	0.92±0.08
SNR candidates	22	34	66
I_{th} 6.3 cm	30	54±8	46±8
I_{nth} 6.3 cm	30	43±8	57±8
I_p 21.1 cm	50	67±8	33±8
I_p 17.4 cm	50	50±8	50±8
I_p 11.1 cm	50	68±7	32±7
I_p 6.3 cm	30	66±6	34±6

emission yields information on the distribution of dust in M 33. This is the subject of a forthcoming paper in this series.

9.2. Origin of cosmic ray electrons

The distribution of the non-thermal emission from M 33 appears to be smoother than that of the thermal emission (Figs. 8, 9 and Berkhuijsen, 1983). This is also the case in M 31 (Beck and Gräve, 1982), NGC 6946 (Klein et al., 1982), M 51 (Klein et al., 1984), IC 342 and M 101 (Gräve, 1984). It should be noted that, in part, the differences in smoothness between the two components may be caused by the assumption of a constant non-thermal spectral index. The derived non-thermal emission of M 33, reflecting the combined distribution of the interstellar magnetic field and the synchrotron emitting electrons, arises from the outer regions and has a maximum southwest of the minor axis. The surface number density of the SNR candidates detected so far is also concentrated to the south (Fig. 9), suggesting that supernova remnants or other objects of the young stellar population could be the main sources of the relativistic electrons.

The radial profiles of both the non-thermal emission and its polarized fraction have scale lengths nearly 3 times larger than those of the two constituents of the young population: thermal emission and SNR candidates (see Table 2). The smooth and extended distribution of the non-thermal emission compared to the much more concentrated SNR candidates suggests that the relativistic electrons leave their discrete places of origin. Assuming energy equipartition between the magnetic field and cosmic rays (see e.g. Klein et al., 1982), an estimate of the cosmic ray electron scale length may be obtained:

$$l_{cr} = 0.5\ (\alpha_{nth} + 3)\ l_{nth} = 7.2 \pm 0.6\,\mathrm{kpc}\,.$$

Hence, on average the electrons apparently propagate radially over a distance l_{cr}–$l_{SNR} \approx 6$ kpc away from their supposed sources, a value consistent with the difference l_{cr}–l_{th} for the Galaxy (Beuermann et al., 1985) and other nearby galaxies studied with somewhat similar resolution to M 33: M 31 (Beck and Gräve, 1982), NGC 6946 (Klein et al., 1982) M 51 (Klein et al., 1984), IC 342 and M 101 (Gräve, 1984), and M 81 (Beck et al., 1985). Beck et al. assume an Alfvén velocity increasing outwards to explain the long distance diffusion within the cosmic ray electron lifetimes. The Alfvén speed in M 33 will be discussed in Paper III. Beuermann et al. (1985) have suggested that the cosmic ray electrons may move by convection and diffusion from the source regions in the thin disk through the thick radio disk back towards the galactic plane, reaching it at a radius larger than that from which they started.

9.3. Star formation

Finally the radio results together with the known optical results will be discussed in terms of two suggested star formation mechanisms. The smooth spiral structure of the blue light indicates that star formation in M 33 takes place both in and between the arms (Elmegreen and Elmegreen, 1984). Note however, that the global and fine structures of M 33 show differences between the northern and southern half.

The northern main arm IN consists of 4 large, intense H II complexes separated by ≈450 pc wide regions of diffuse emission (Dubout-Crillon, 1977) with gas and dust situated on the outer edges (Humphreys and Sandage, 1980). The gas in IN may rotate too fast for the production of a density wave shockfront (Dubout-Crillon, 1977).

The southern main arm IS contains H I, dust, O stars and small, intense H II regions concentrated in a ridge 100 pc wide and 4 kpc long along the inside edge (Dubout-Crillon, 1977; Boulesteix et al., 1981). Arm IS has twice as many early type stars (Dubout-Crillon, 1977) and an integrated Hα flux three times higher than that of IN (Boulesteix et al., 1981).

Radial distributions of the number surface density of SNR candidates and the polarized emissions at 6.3 cm and 17.4 cm are relatively high near $r = 13'$ (2.7 kpc). The thermal emission derived from the Hα catalogue also shows a slightly increased value at this radius (see Fig. 1 in Berkhuijsen and Klein, 1985). Newton's (1980) neutral hydrogen map has a distinct minimum at $r = 13'$ with average emission 30% lower than at adjacent radii. On the other hand, the recent H I map of Deul and van der Hulst (1987) with four times higher resolution and correction of missing spacings shows generally low emission between $r = 11'$ and $r = 16'$, but a local maximum around $r = 14'$.

At $r = 13'$ the two-arm spiral structure terminates and the corotation radius is assumed (Roberts et al., 1975) that would introduce a break in many distributions. The deviations at $r \approx 13'$ could be interpreted as enhanced star formation which would in turn cause a general depletion of the H I, enhanced thermal emission and finally more supernova remnants. However, according to the density wave theory, the relative velocity between the gas and the density wave becomes zero at the corotation radius and neither a shock nor star formation is expected there.

Alternatively, Kaufman (1981) explained the spiral structure of M 33 by at least one weak density wave within 2.8 kpc and stochastic self-propagating star formation (SSPSF) over the whole galaxy. This could not only account for the $r = 13'$ deviations but also for the formation of the brightest H II region, NGC 604, situated at the slightly larger distance of 3 kpc.

In any case, the stronger polarized emission at $r = 13'$ is surprising, because increased non-thermal emission is neither visible with the current resolution (Fig. 10) nor in the profile of Berkhuijsen and Klein (1985). Thus one must adopt there either a large uniformity of the magnetic field or little Faraday depolarization. Both assumptions are unsatisfactory since (i) star formation would perturb the interstellar medium, and (ii) in-

Table 4. Positions of five 2.8 cm radio continuum maxima, related spiral arms, possible coincidences "+" with dust patches and identifications with H II regions (Viallefond et al., 1986, VGHC) or SNR candidates (D'Odorico et al., 1982, DDB)

Peak	α_{50}	δ_{50}	arm	dust	VGHC	DDB
P1	$1^h30^m.7$	30°17'	IS	+	40,48	–
P2	1 30.9	30 18	IS	-	–	–
P3	1 31.1	30 18	IS?	-	69	9
P4	1 31.4	30 19	IVS/VS	+	94,99	–
P5	1 31.4	30 21	IVS	+	92,95	–

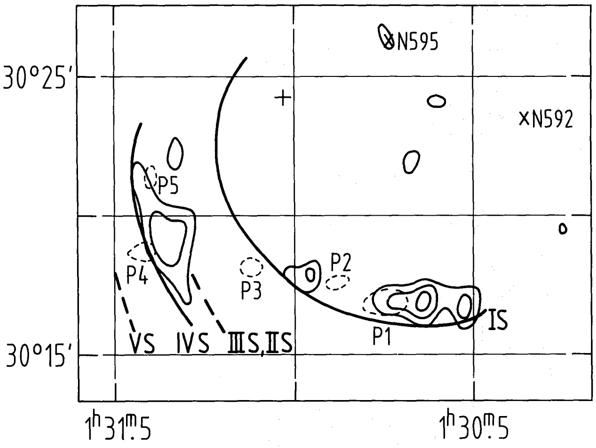

Fig. 12. Comparison of radio continuum peaks P 1–P 5 at 2.8 cm (dashed, from Fig. 4) with integrated H I (Plate 4 in Newton, 1980). H I contours are at 872, 1163, and 1454 K km s^{-1}. Arm structure is taken from Humphreys and Sandage (1980, Fig. 24)

creased thermal emission would lead to higher Faraday depolarization.

The northern half of M 33 is more ordered than the southern half: at 6.3 cm the 4 outer radio continuum arms are more clearly visible (Fig. 3), H I spiral features in the outer regions are more pronounced (Newton, 1980) and linear polarization is detectable in the northwestern quadrat (Paper I). Otherwise, neither the optical nor the radio emission shows any indication of density waves.

In the SW, the distinct lack of OB stars (cf. Fig. 5 in Berkhuijsen, 1983) in the vicinity of the assumed corotation radius is in agreement with the density wave theory. The brighter radio luminosity of arm IS visible here at 6.3 cm and 2.8 cm compared to IN (Sect. 2) is attributed by Berkhuijsen (1983) solely to increased non-thermal emission. The non-linear density wave theory (Roberts and Yuan, 1970) predicts more intense non-thermal emission inside the corotation radius at the inner edges of the arms. This could be the case in the southern regions of M 33, where the radio continuum emission peaks generally occur ≈200 pc towards the inner edges of the nearest optically bright regions (Figs. 3 and 4). At 2.8 cm only ≈ 50% of the total intensity is non-thermal. The resolution of the available spectral index distribution is not sufficient for a detailed separation of the radio continuum, thus prohibiting classification of its origin.

Approaching the centre it becomes difficult to distinguish between the southern arms IIS to VS (Ivanov and Kunchev, 1985, e.g. fit the M 33 OB associations with only seven spiral arms!). Therefore the definition of the positions of the 5 radio continuum peaks (Table 4) relative to the arms becomes uncertain. Figure 12 relates the 5 maxima to the H I peaks (Newton, 1980, Plate 4) and the arm structure of Humphreys and Sandage (1980). P 3, situated to the outside or on IS, is consistent with the shell type SNR DDB 9 (D'Odorico et al., 1982) that has been resolved with the VLA at 20 cm (Goss and Viallefond, 1985) and detected in X-rays (Markert and Rallis, 1983). P 1, P 4, and P 5 include known H II regions (Viallefond et al., 1986) within the 2.8 cm beam. The peaks tend to coincide with low H I density. On a more general scale Viallefond and Goss (1986) found optical and radio H II regions to be related to H I concentrations. Humphreys and Sandage (1980, Fig. 25) also established the distribution of dust patches in M 33. It appears that the maximum radio continuum (P 1 and P 2), H I and possibly dust (Table 4) occur on the same line along the inside of IS. P 5 lies to the inside of IVS in line with H I and dust. P 4 lies on IVS or inside VS together with dust.

Pecularities in the radial profiles and the radio continuum peak positions in the south are consistent with the density wave model of Roberts et al. (1975): a trailing spiral strucure with a corotation radius around $r = 13'$. Based on the polarization data (Paper I), the action of density waves and SSPSF will be studied in terms of the uniformity of the magnetic field in Paper III.

Acknowledgements. I am grateful to Dr. E.M. Berkhuijsen for guidance of the M 33 studies. Drs. J.I. Harnett and R. Beck gave helpful comments on the manuscript.

References

Beck, R.: 1979, Ph.D. Thesis, Rheinische Friedrich-Wilhelms-Universität Bonn
Beck, R.: Gräve, R.: 1982, *Astron. Astrophys.* **105**, 192
Beck, R., Klein, U., Krause, M.: 1985, *Astron. Astrophys.* **152**, 237
Berkhuijsen, E.M.: 1983, *Astron. Astrophys.* **127**, 395
Berkhuijsen, E.M., Klein, U.: 1985, *IAU Symp.* **106**, 431
Beuermann, K., Kanbach, G., Berkhuijsen, E.M.: 1985, *Astron. Astrophys.* **153**, 17
Blair, W.P., Kirshner, R.P.: 1985, *Astrophys. J.* **289**, 582
Boulesteix, J., Courtés, G., Laval, A., Monnet, G., Petit, H.: 1974, *Astron. Astrophys.* **37**, 33
Boulesteix, J., Dubout-Crillon, R., Monnet, G., Petit, M., Lombard, J.: 1981, *Astron. Astrophys.* **104**, 15
Buczilowski, U.R.: 1985, Ph.D. Thesis, Rheinische Friedrich-Wilhelms-Universität Bonn

Buczilowski, U.R.; Beck, R.: 1987, *Astron. Astrophys. Suppl.* **68**, 171 (Paper I)

Bystedt, J.E.V., Brinks, E., Bruyn, A.G. de, Israel, F.P., Schwering, P.B.W., Shane, W.W., Walterbos, R.A.M.: 1984, *Astron. Astrophys. Suppl.* **56**, 245

Colin, J., Athanassoula, E.: 1981, *Astron. Astrophys.* **97**, 63

Courtés, G., Petit, H., Sivan, J.-P., Dodonov, S., Petit, M.: 1987, *Astron. Astrophys.* **174**, 28

Deul, E.R., Hulst, J.M. van der: 1986, Annual Report 1985 of Netherlands Foundation for Radio Astronomy, p. 159

Deul, E.R., Hulst, J.M. van der: 1987, *Astron. Astrophys. Suppl.* **67**, 509

D'Odorico, S., Dopita, M.A., Benvenuti, P.: 1980, *Astron. Astrophys. Suppl.* **40**, 67

D'Odorico, S., Goss, W.M., Dopita, M.A.: 1982, *Monthly Notices Roy. Astron. Soc.* **198**, 1059

Dopita, M.A., D'Odorico, S., Benvenuti, P.: 1980, *Astrophys. J.* **236**, 628

Dubout-Crillon, R.: 1977, *Astron. Astrophys.* **56**, 293

Elmegreen, D.M., Elmegreen, B.G.: 1984, *Astrophys. J. Suppl.* **54**, 127

Gioia, I.M., Gregorini, L., Klein, U.: 1982, *Astron. Astrophys.* **116**, 164

Goss, W.M., Viallefond, F.: 1985, *J. Astron. Astrophys.* **6**, 145

Gräve, R.: 1984, Ph.D. Thesis, Rheinische Friedrich-Wilhelms-Universität Bonn

Hummel, E.: 1981, *Astron. Astrophys.* **93**, 93

Humphreys, R.M., Sandage, A.: 1980, *Astrophys. J. Suppl.* **44**, 319

Israel, F.P., Hulst, J.M. van der: 1983, *Astron. J.* **88**, 12, 1736

Ivanov, G.R., Kunchev, P.Z.: 1985, *Astrophys. Space Sci.* **116**, 341

Kap-herr, A. von, Berkhuijsen, E.M., Wielebinski, R.: 1978, *Astron. Astrophys.* **62**, 51

Kaufman, M.: 1981, *Astrophys. J.* **250**, 534

Klein, U., Beck, R., Buczilowski, U.R., Wielebinski, R.: 1982, *Astron. Astrophys.* **108**, 176

Klein, U., Emerson, D.T.: 1981, *Astron. Astrophys.* **94**, 29

Klein, U., Urbanik, M., Beck, R., Wielebinski, R.: 1983, *Astron. Astrophys.* **127**, 177

Klein, U., Wielebinski, R., Beck, R.: 1984, *Astron. Astrophys.* **135**, 213

Markert, T.M., Rallis, A.D.: 1983, *Astrophys. J.* **275**, 571

Newton, K.: 1980, *Monthly Notices Roy. Astron. Soc.* **190**, 689

Reynolds, J.E., Harnett, J.I.: 1983, *Proc. Astron. Soc. Aust.* **5,2,** 235

Roberts, W.W., Roberts, M.S., Shu, F.H.: 1975, *Astrophys. J.* **196**, 381

Roberts, W.W., Yuan, C.: 1970, *Astrophys. J.* **161**, 881

Vaucouleurs, G. de: 1978, *Astrophys. J.* **223**, 730

Vaucouleurs, G. de, Leach, R.W.: 1981, *Publ. Astron. Soc. Pacific* **93**, 190

Viallefond, F., Goss, W.M.: 1986, *Astron. Astrophys.* **154**, 357

Viallefond, F., Goss, W.M., Hulst, J.M. van der, Crane, P.C.: 1986, *Astron. Astrophys. Suppl.* **64**, 237

Webber, W.R., Simpson, G.A., Cane, H.V.: 1980, *Astrophys. J.* **236**, 448

Wright, M.C.H., Warner, P.J., Baldwin, J.E.: 1972, *Monthly Notices Roy. Astron. Soc.* **155**, 337